Journal of CO_2 Utilization 36 (2020) 244–252

Contents lists available at ScienceDirect

Journal of CO_2 Utilization

journal homepage: www.elsevier.com/locate/jcou

Catalytic CO_2 absorption in an amine solvent using nickel nanoparticles for post-combustion carbon capture

Seokju Seo, Brian Lages, Myeongsub Kim*

Department of Ocean and Mechanical Engineering, Florida Atlantic University, 777 Glades Road, Boca Raton, FL33431, USA

ARTICLE INFO

Keywords:
CO_2 absorption
Carbon capture
Microfluidics
Monoethanolamine
Nickel nanoparticles

ABSTRACT

In industrial post-carbon capture processes, monoethanolamine (MEA) has been mainly used as an absorption solvent. However, this approach generates significant amounts of toxic wastewater containing a heavy chemical difficult to treat and also raises concerns about acute corrosion of metal structures in the facility. To reduce the use of MEA in carbon capture, this work evaluates the catalytic performance of nickel nanoparticles (NiNPs) for CO_2 capture as a possible additive in an MEA solvent. We test the CO_2 absorption rate in MEA catalyzed by NiNPs in both limited and high mixing conditions to model real capturing processes in the packed column of industrial absorption reactors. For this purpose, a microreactor and a long serpentine microchannel are employed. The catalytic absorption performance of NiNPs for CO_2 in aqueous MEA is evaluated using CO_2 microbubbles by monitoring changes in size upon their time-dependent absorption. We find that the average CO_2 absorption rate with NiNPs is accelerated by 34% in the limited mixing condition in the microreactor. This increase is mainly due to NPs' catalytic CO_2 absorption driven by a Brownian motion. On the other hand, in the high mixing condition in the long serpentine microchannel, the catalytic activity of NiNPs improves the average CO_2 absorption rate further to 54%. This improvement makes it possible to shorten the timescale for reaching CO_2 absorption equilibrium and therefore to reduce the size of the reactors significantly. The test results demonstrate that NiNPs serve as suitable additives in the MEA-based CO_2 absorption system.

1. Introduction

Over the last 150 years, the consumption of petroleum energy reserves has been continuously increased to meet global fuel demands for power generation. Due to the combustion processes for fossil fuels, atmospheric emissions of greenhouse gas, particularly carbon dioxide (CO_2), have been rapidly doubled for the last four decades. The increased greenhouse gas emissions cause serious international concerns about global warming, sea-level rise, and ocean acidification. Post-carbon capture technology that separates CO_2 from flue gas in fossil fuel-fired power plants has contributed to the significant migration of atmospheric CO_2 emissions. The post-carbon capture can be accomplished by several approaches including chemical and physical absorption [1], adsorption [2], cryogenics [3], membranes [4], and biological separation methods [5]. Among these options, amine scrubbing and stripping using solvent absorption of CO_2 are the only technology conveniently retrofitted to the existing power plants. The most dominant absorption solvent is the amine derivatives because of their superior absorption efficiency, fast reaction kinetics, and low costs [6]. Specifically, monoethanolamine (MEA), diethanolamine, methyl diethanolamine, and 2-amino-2-methyl-1-propanol have been dominantly used in most industrial applications [7,8]. As a result, the consumption of ethanolamine (EA) has been significantly escalated as increasing the demand for CO_2 capture [9–12]. For example, the EA market in North America has accounted for revenue of $794 million in the year 2017 and is expected to grow at $1224 million by the year 2025 [13].

The huge consumption of EA has been significantly escalated as increasing the demand for CO_2 capture [9–12]. The use of EA in post-combustion CO_2 capture processes creates several concerns and challenges. First, it is known that the amine-based carbon capture produces a large amount of wastewater. For example, EA at high concentrations in the solvent increases chemical oxygen demand and total nitrogen induced by its bifunctional properties of the primary alcohol and amine [10,11,12]. To treat wastewater containing the amine solvent, various techniques including ozonation chemical processes [14], electrodialysis reversal with electrolysis [15], microbial electrochemical system [11,12,16], fluidized-bed Fenton technology [17] and titanium dioxide (TiO_2) photocatalyzed oxidation [18] have been suggested. However, these processes involve high energy consumption and expensive

* Corresponding author.
E-mail address: kimm@fau.edu (M. Kim).

https://doi.org/10.1016/j.jcou.2019.11.011
Received 21 August 2019; Received in revised form 21 October 2019; Accepted 8 November 2019

treatment processes. Second, corrosive fume is generally released during the solvent regenerative processes due to the acid gas that the amine absorbs [19,20]. Also, it is very susceptible to occur corrosion in carbon steel exchangers, condensers, and reboiler-type bundles [21]. Therefore, EA concentrations are typically limited to 15 − 30 wt% in the power plant facilities to avoid wastewater and corrosion issues [22]. Third, to achieve high capturing efficiency at a low concentration of the amine solvent, a regeneration process that involves a stripper column with reflux and reboiler sections is necessary [23]. However, these operational requirements make the amine-based CO_2 capture complicated and expensive [8].

As a result of increased environmental and energy concerns, many additives in the amine-based CO_2 capture have been developed for the enhancement of CO_2 absorption. The application of amine blends as absorbent is commonly used to accelerate the CO_2 absorption rate in traditional amine solvents [24]. Especially, the amino acid ionic liquid (AAIL), such as 1-butyl-3-methylimidazolium glycinate ([Bmim][Gly]), 1-butyl-3-methylimidazolium lysinate ([Bmim][Lys]) and tetramethylammonium glycinate ([N1111][Gly]) has been attempted to improve the CO_2 absorption performance [24–26]. The addition of AAIL into the MDEA aqueous solution significantly improves the CO_2 removal efficiency and overall volumetric mass transfer coefficient in the order of [N1111][Gly] > [Bmim][Lys] > [Bmim][Gly]. As another approach to improve the CO_2 absorption performance, catalytic additives for enhanced CO_2 absorption such as the zinc(II) and cobalt (III) complexes [27], boric acid [28], and carbonic anhydrase [29] have been employed. These catalysts increase the CO_2 absorption rate greatly and therefore help reduce the operating costs and the amount of the amine solvent. Besides, the improved absorption efficiency facilitates the reduction of the CO_2 absorber size [29].

Compared with the aforementioned additives, nickel nanoparticles (NiNPs) could be a suitable additive for carbon capture in the MEA solvent that satisfies the requirements. To suit the catalytic additives to the amine scrubbing and stripping processes, the following required properties are desired. First, superior corrosion resistance to EA is required to avoid degradation of its catalytic characteristics. Ni element is a ductile transition metal that is generally considered corrosion-resistant [30]. Second, high-temperature resistance is needed during the regeneration process due to its high operation temperature [31]. NiNPs have high resistance to deformation induced by high-temperature conditions in the amine regeneration process because the initiation of oxidation altering NiNPs' characteristics occurs at approximately 300 °C [32]. Since the temperature of stripper and reboiler is no more than 120 °C in practical applications [33], the thermal degradation of NiNPs by high-temperature is unlikely to occur. Lastly but most importantly, the pH-independent performance is required because the solution pH rapidly decreases as CO_2 is continuously dissolved during carbon capture [7]. Unlike many leading catalysts, e.g., arsenate, borate, carbonic anhydrase enzyme, and selenite [34], NiNPs maintain their catalytic performance consistent regardless of pH [35–37].

Here, we examined the catalytic performance of NiNPs as additives for enhanced CO_2 absorption in an amine-based solvent. Their catalytic activity in different mixing conditions., i.e., the limited and high mixing was thoroughly studied because the mixing scale inside the actual CO_2 absorber column varies depending on the design of the chemical solvent absorption process. To study the absorption reactions in different mixing conditions, a microfluidic technique that provides excellent controllability of reaction times and mixing scales of multiphase flows was employed. The rates of CO_2 absorption across the gas/liquid interface were quantified via changes in the size of a series of spherical microbubbles.

2. Materials and methods

2.1. Materials

Monoethanolamine (≥ 99% purity), NiNPs powder (≥ 99% purity, < 100 nm average particle size), phosphate buffer powder, and sodium dodecyl sulfate (SDS, > 99% purity) were purchased from Alfa Aesar (Ward Hill, MA) and Sigma − Aldrich (St. Louis, MO), respectively. PDMS elastomer kits (Sylgard 184) were purchased from Dow Corning Corp. (Midland, MI) for preparing microfluidic devices.

2.2. Microfluidic device fabrication

The standard soft lithography method was used to fabricate the microfluidic chips. The designs of microchannel geometries were drawn with computer-aided design (CAD) software (AutoCAD 2017, Autodesk, Inc., Sausalito, CA). The geometry designs were printed at a high resolution (25,400 dpi, CAD/ART Services Inc., Bandon, OR) on a transparency sheet to make a patterned photomask. The UV light was exposed to a layer of negative photoresist (KMPR 1025, Microchem, Newton, MA) coated on a silicon wafer (UniversityWafer, Inc., Boston, MA). Photomask patterns were transferred to the silicon wafer creating a master mold. Poly(dimethylsiloxane) (PDMS) and its cross-linker were mixed at a ratio of 10:1 (weight:weight). After degassing using a vacuum pump, this mixture was poured onto the master mold. The cured PDMS layer was peeled off the mold after curing in an oven at 70 °C for 1 h. We made inlet and outlet ports on the PDMS layer using a 1.0 mm diameter biopsy punch (Integra Miltex, Inc., Germany). The PDMS layer and glass microscope slide (25 × 75 × 1.0 mm, Fisher Scientific, Fair Lawn, NJ) were bonded by an oxygen plasma treatment (Harrick Plasma, Ithaca, NY). Furthermore, this process changes the surface of the microchannel to hydrophilic which makes water wet of the surface so that CO_2 bubbles remain in the liquid phase.

2.3. Configuration of reactors

To model dynamic CO_2 reactions with the aqueous-amine solution in the industrial absorbers, two different mixing conditions were considered. Fig. 1 shows schematic diagrams of these test platforms and associated approaches for the evaluation of CO_2 capture performance: a microreactor for the limited mixing condition (Fig. 1a) and a long serpentine microchannel for the high mixing condition (Fig. 1b). In both geometries, a series of CO_2 microbubbles was generated in a flow-focusing geometry consisting of two inlets (a continuous phase on both side channels) and one outlet (a discrete phase in the center channel). The width (W_a) of the aqueous solutions and the downstream is 100 μm and the width (W_g) of the CO_2 gas channel is 50 μm. The height (h) of all microchannels is 75 μm.

2.4. Experimental setup and procedure

One mM PBS was prepared using ultrapure water (resistivity 18.2 MΩ cm) obtained from a Millipore Milli-Q integral 5 purification system (Millipore, Bedford, MA). SDS at a concentration of 625 mg/L was used to enhance the stability of CO_2 bubbles: SDS helps significantly avoid the coalescence of bubbles due to their collision and the burst of bubbles [38]. While the concentration of SDS was kept constant in all experiments, the concentration of MEA in the continuous phase was varied as a control parameter (Fig. 1). Except for the experiment on NiNPs' dissolution in an aqueous MEA solution, the concentration of NiNPs was kept constant to be 30 mg/L in all experiments that creates the maximum NPs' catalytic performance of CO_2 capture in pure water derived from our previous study [36]. Suspension of 1000 mg L^{-1} NiNPs with 10% MEA was used for absorbance measurements due to the limit of detection in the UV–vis spectrophotometer (Evolution 201, Thermo Scientific, Waltham, MA). To study the authentic effect of

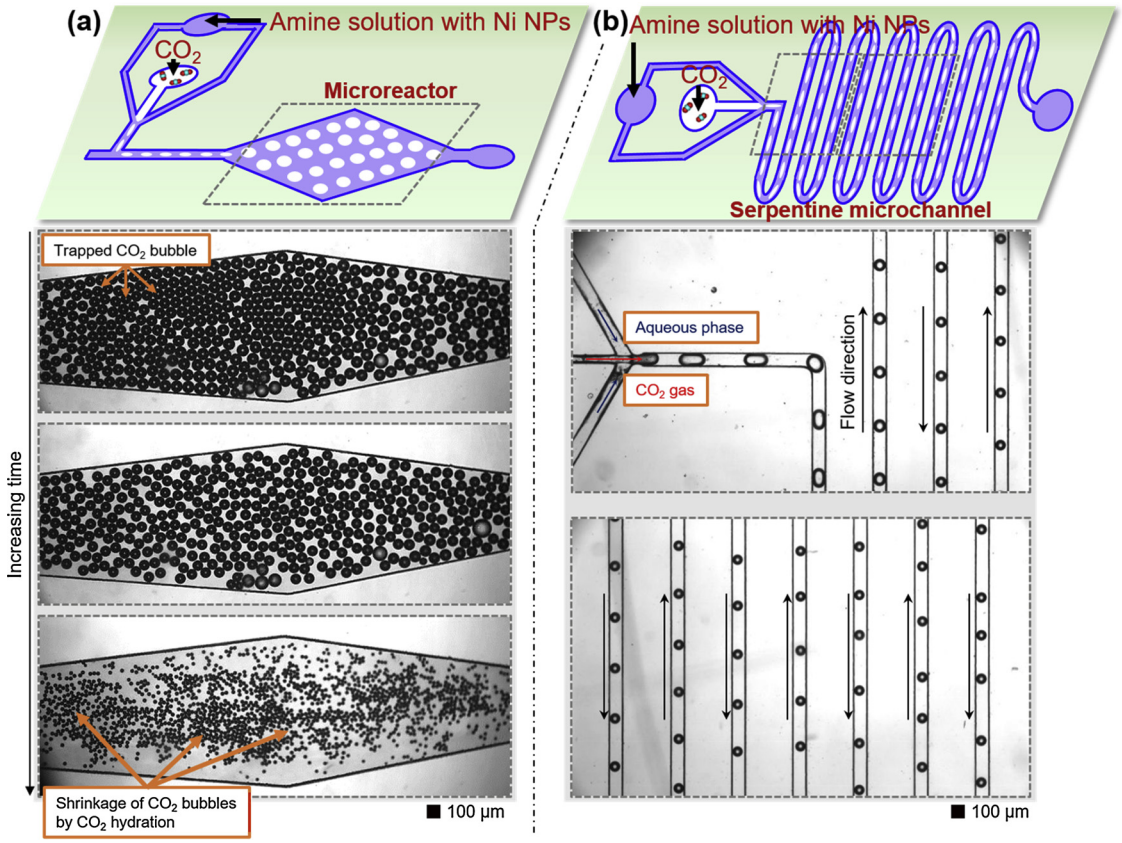

Fig. 1. Schematic of the microfluidic approaches for evaluation of CO_2 absorption. (a) Design of a microreactor under the limited mixing condition and sequential images of changes in CO_2 microbubble size. (b) Design of a long serpentine microchannel under the high mixing condition and images of CO_2 microbubbles at two different locations. A scale bar represents 100 μm.

NiNPs' catalytic performance for CO_2 absorption in the amine solvent under the limited mixing condition (Fig. 1a), four different experimental conditions were tested. In the presence and absence of NiNPs, 0 and 10% MEA with SDS were tested. On the other hand, in the chaotic mixing condition (Fig. 1b), NiNPs' catalytic performance was tested at 0, 1.25, 5, and 10% MEA with SDS. All experiments were carried out at room temperature of 25 °C under ambient pressure. The test solutions were introduced to the microfluidic chip at a flow rate of 0.3 mL/min through PTFE (polytetrafluoroethylene) tubing using a syringe pump (PHD ULTRA 4400, Harvard Apparatus, Natick, MA). The pure CO_2 gas was introduced to the chip at 1 psi using a precise gas controller (Alicat Scientific, Tucson, AZ) connected to a CO_2 cylinder (99.9% purity, Airgas, USA) through PTFE tubing. Optical microscopy images of CO_2 microbubbles under different experimental conditions were captured using a high-speed camera (1920 × 1080-pixel resolution, 400 Hz frame rate, 12-bit depth; Fastec IL5S, Fastec Imaging Corp., San Diego, CA) attached to an inverted microscope (IX73, Olympus Corp., Japan) with a 4x objective lens (Numerical Aperture = 0.13, UplanFLN4X, Olympus Corp., Japan). A halogen lamp (a 100 W, 12 V, U-LH100-3, Olympus Corp., Japan) was used as a light source. Because the interface between gas and liquid appears dark, a binary function in the ImageJ software, an open-source image processing program, was used for estimating the CO_2 bubble size.

3. Results and discussion

3.1. CO_2 absorption by NiNPs in a microreactor

The CO_2 absorption into the aqueous solvent is governed by Henry's law:

$$CO_{2(g)} + H_2O \overset{k_H}{\leftrightarrow} CO_{2(aq)}, \left(k_H = \frac{P_{CO_2}}{[CO_2]_{aq}}\right) \quad (1)$$

where P_{CO2} is the partial pressure of gaseous CO_2, k_H is the Henry's constant for CO_2 in pure water (3.45×10^3 kPa L/mol), and $[CO_2]_{aq}$ is the concentration of dissolved CO_2 in the aqueous phase. Based on Henry's law, the size of CO_2 bubbles will be decreased as the mass transfer from the gas to aqueous phases increases. In other words, visualization of CO_2 bubbles in an aqueous solution at different times provides a unique venue to estimate the rate of CO_2 diffusion into the water and therefore overall CO_2 absorption. Besides, it is known that the mass transfer of CO_2 from a gas phase to an aqueous phase increases as a mixing rate of the aqueous phase is increased [39]. This suggests that the rate of physical absorption of gaseous CO_2 into the aqueous phase in the microreactor (i.e., limited mixing condition) is expected to be lower than that in the serpentine channel (i.e., high mixing condition) due to the difference in the degree of mixing.

To test the feasibility of the estimation of absorption performance using size variations in CO_2 bubbles, the changes in the size of CO_2 microbubbles in the limited stirring condition (i.e., CO_2 microbubbles in a microreactor) were examined. This method also provides a way to estimate the catalytic performance of NiNPs as effective additives for improved CO_2 absorption. We first tested the CO_2 absorption rate in pure water in order to evaluate NiNPs' intrinsic catalytic properties. Fig. 2a shows representative images of CO_2 microbubbles in the aqueous solution entering the microreactor. To generate a series of microbubbles in uniform size, the inlet pressure of CO_2 gas and the flow rate of the aqueous solution were maintained constant over the entire test. Since the reaction of gaseous CO_2 with the aqueous solution occurs immediately after the bubble formation, the geometry (the microreactor + the flow-focusing structure) was designed to collect CO_2

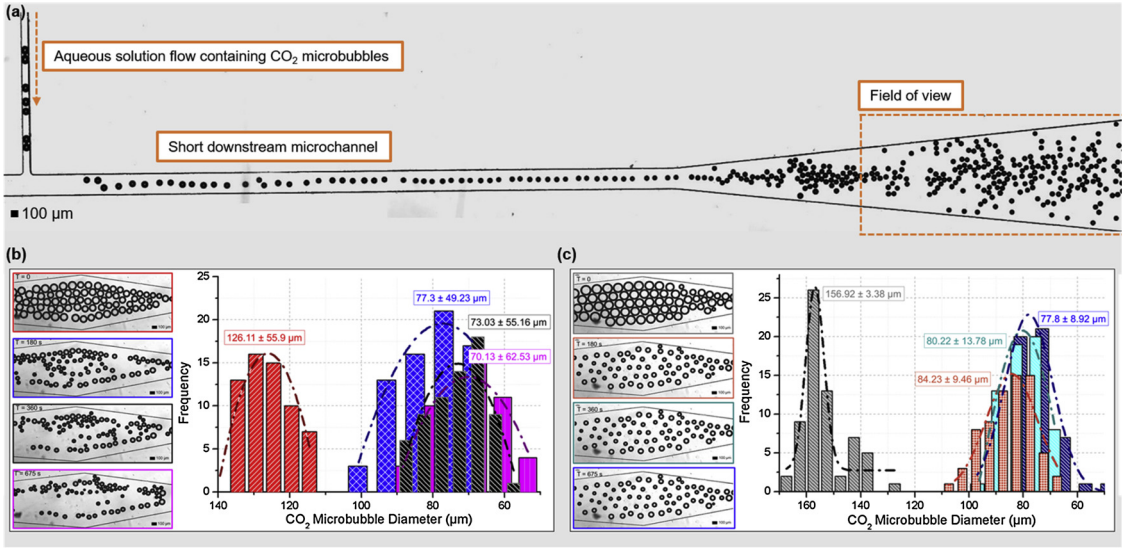

Fig. 2. (a) A representative microscopy image of CO_2 microbubbles in the aqueous solution in a microreactor. (b, c) Statistical distributions of microbubble's diameters in the (b) absence and (c) presence of NiNPs. These diameters were determined from sequential images of changes in CO_2 bubble size at different times. The numbers in (b, c) represent an average diameter ± standard deviation. The bin size for all histograms is 5 − 10 μm and a scale bar is 100 μm.

microbubbles in the microreactor at a short retention time. Once a number of CO_2 microbubbles were sufficient to fill-up the microreactor, CO_2 gas and the solution were instantly stopped together by controlling a solenoid valve. After collecting a number of CO_2 bubbles, we observed the changes in their size when the physical absorption of CO_2 (g) into the surrounding aqueous solvent occurs. Figs. 2b and 2c present sequential images of changes in CO_2 microbubbles in the absence and presence of NiNPs in the microreactor, respectively. Statistical distributions of bubble diameters at different times were obtained from more than 50 CO_2 bubbles (Figure S1 and S2). The average bubble diameters were estimated using a curve-fit to the Gaussian function and the average diameters with the standard deviations were determined to be 126.11 ± 55. 9 (156.92 ± 3.38), 77.3 ± 49.23 (84.23 ± 9.46), 73.03 ± 55.16 (80.22 ± 13.78), and 70.13 ± 62.53 (77.8 ± 8.92) μm at time t = 0, 180, 360, and 675 s in the absence and (presence) of NiNPs. The faster decrease of bubble size can be explained by the catalytic reaction between NiNPs and water molecule. It has been known that NiNPs accelerate the mass transfer of gaseous CO_2 into the aqueous solution as a result of their catalytic activity [36,37]. A single NiNP in the water reacts with a water molecule to form a hydroxyl group (OH-) on its surface.

$$Ni\,NP + H_2O \rightarrow Ni\,NP - OH^- + H^+ \quad (2)$$

Then, OH- reacts with CO_2 (aq) to form bicarbonate (HCO_3-).

$$Ni\,NP - OH^- + CO_2(aq) \rightarrow Ni\,NP - HCO_3^- \quad (3)$$

HCO_3- is replaced by H_2O and dissociates further into H^+ and CO_3^{2-} ions.

$$Ni\,NP - HCO_3^- + H_2O \rightarrow Ni\,NP - H_2O + HCO_3^- \quad (4)$$

This series of reactions accelerates the formation of HCO_3- ion near surrounding CO_2 microbubbles thereby increasing the rate of shrinkage of the bubble size.

3.2. CO_2 absorption by NiNPs and MEA in a microreactor

To understand how effectively NiNPs accelerate CO_2 absorption in an amine-based solvent, quantitative analysis of changes in CO_2 bubble size was carried out in the aqueous solution containing 10% MEA with and without NiNPs. The microfluidic chip used in this test is a microreactor because the CO_2 absorption was observed in the limited mixing condition. Fig. 3 summarizes the experimental results for the relative changes in the CO_2 bubble size in the pure water (Fig. 3a) and aqueous MEA (Fig. 3b) with and without NiNPs, respectively. Fig. 3a shows that the rate of CO_2 absorption in the aqueous-NiNPs solution was slightly improved; it takes 300 s to reach a 40% decrease in the size of microbubbles in the pure aqueous solution while it takes 100 s with NiNPs. This infers that the time to reach equilibrium in the aqueous-NiNPs solution is slightly decreased due to the limited catalytic activity of NiNPs when compared with that in the pure water. This behavior can be explained by the Brownian motion of NPs. When there is no external disturbance, the Brownian motion of NPs (which occurs when NPs are bombarded by fluid particles) is mainly responsible for their movement inside the microreactor [40,41]. NiNPs' surface reaction is activated by physical contact between NiNPs and CO_2 (aq) molecules, mainly driven by the Brownian motion, and therefore induces increased CO_2 absorption. Based on the Stokes-Einstein equation, the value of NPs' translational diffusion coefficient (D_T) defines the velocity of Brownian motion: $D_T = k_B T/3\pi\eta d_H$, where D_T is the translational diffusion coefficient (m^2/s), k_B is the Boltzmann's constant, T is the absolute temperature, η is the dynamic viscosity, and d_H is the hydrodynamic diameter which is determined by a dynamic light scattering system, Zetasizer Nano ZS90 (Malvern Instruments, UK). The D_T of 30 mg/L NiNPs was determined to be 0.277 $\mu m^2/s$.

Fig. 3b shows the changes in normalized CO_2 bubble diameter in aqueous MEA with and without NiNPs. Owing to MEA's excellent CO_2 absorption capacity, initial CO_2 bubbles were disappeared within 40 s inside the microreactor. This rapid decrease in microbubble size can be explained by the chemical reaction between MEA and CO_2 in addition to the CO_2-H_2O reaction. CO_2 is absorbed in aqueous MEA accompanied by the accelerated dissolution of CO_2 in H_2O to form HCO_3- by the NiNPs' catalytic activity. When CO_2 is injected into the aqueous MEA solution, MEA is bound with CO_2 to form MEA-CO_2 zwitterion (MEA^+COO-) [42,43].

$$MEA + CO_{2(aq)} \overset{k_1,\ k_{-1}}{\leftrightarrow} MEA^+COO^-$$

Then, MEA^+COO- is deprotonated by H_2O to generate the carbamate (MEACOO-) and hydronium (H_3O^+). k_1 and k_{-1} are the second-order forward and backward rate coefficients for the reaction.

$$MEA^+COO^- + H_2O \rightarrow MEACOO^- + H_3O^+ \quad (6)$$

Another MEA molecule reacts with MEACOO- and H_3O^+ to form the protonated MEA.

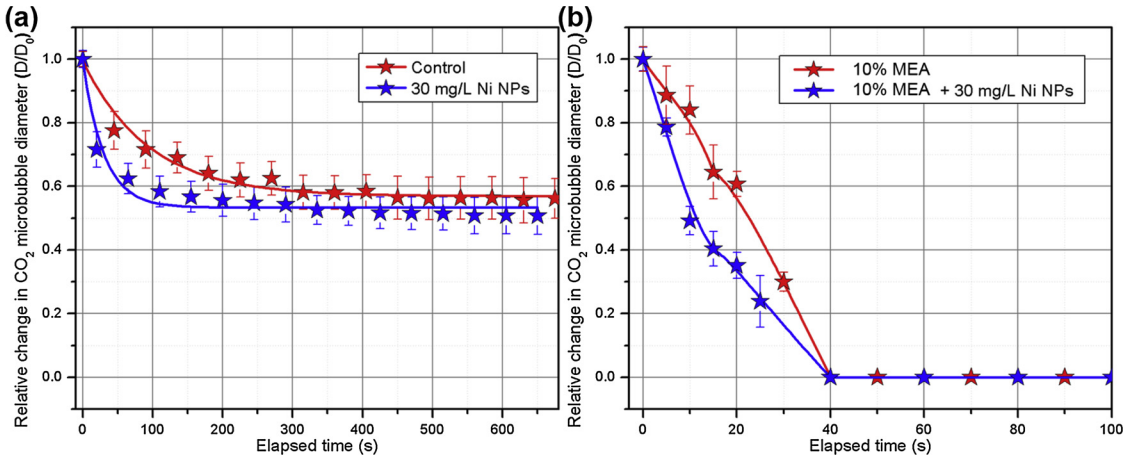

Fig. 3. Graphs for relative changes in CO_2 bubble diameter in (a) water and (b) 10% aqueous MEA with (★) and without (★) NiNPs. Each data point and error bar in the graph are obtained from fifty measurements under each experiment condition.

$$MEA + MEACOO^- + H_3O^+ \rightarrow MEAH^+ + H_2O + MEACOO^- \quad (7)$$

Then, MEACOO- reacts with H_3O^+ to generate carbamic acid (MEACOOH).

$$MEACOO^- + H_3O^+ \rightarrow MEACOOH + H_2O \quad (8)$$

These additional cascade MEA-CO_2 reactions lead to the rapid removal of aqueous CO_2 and therefore an increase in the gaseous CO_2 absorption. From the zwitterion mechanism, the MEA reaction rate of CO_2 is described as follows [44,45]:

$$r_{CO_2} = \frac{[CO_2]\,[MEA] - \frac{k_{-1}}{k_1}[MEACOO^-]\frac{\sum k_{-b}[MEAH^+]}{\sum k_b[B]}}{\frac{1}{k_1} + \frac{k_{-1}}{k_1 \sum k_b[B]}}$$

where r_{CO2} is the overall CO_2 absorption rate, k_b and k_{-b} are the second-order forward and the backward rate coefficient for the reaction of the base (amine, H_2O, or OH- denote as B). Since the reaction of deprotonated MEA^+COO^- by H_2O to generate $MEACOO^-$ is very fast, $k_{-1}/k_1[MEACOO^-](\Sigma k_{-b}[MEAH^+])/(\Sigma k_b[B])$ is negligible and thereby the overall CO_2 absorption rate can be simplified as follows:

$$r_{CO_2} = \frac{[CO_2]\,[MEA]}{\frac{1}{k_1} + \frac{k_{-1}}{k_1 \sum k_b[B]}}$$

Because the reverse rate of reaction between MEA and CO_2 is much faster than MEA^+COO^- formation ($1/k_1 >> k_{-1}/(k1\Sigma k_b[B])$, the overall CO_2 absorption rate can be further simplified as follows:

$$r_{CO_2} = k_1[CO_2]\,[MEA]$$

Since the reaction rate is to be the first order with respect to the concentration of MEA and CO_2 according to this equation, the higher MEA concentration allows faster reactions with CO_2 and leading rapid shrinkage of CO_2 bubbles.

In Fig. 3b, aqueous MEA with and without NiNPs reaches the CO_2 absorption equilibrium simultaneously at 40 s. However, the rate of CO_2 bubble shrinkage was increased in the presence of NiNPs. Specifically, we estimated the rate of size changes (and therefore the rate of CO_2 diffusion) was increased from 40% without NiNPs to 60% with NiNPs over the first 10 s of the tests. This suggests that even though there is a limited mixing condition inside the microreactor inducing the limited diffusive transport, NiNPs still maintain their catalytic ability due to their free movement by the Brownian motion. We estimated the translational diffusion coefficient of NiNPs in aqueous MEA to be 0.285 $\mu m^2/s$, similar to that of NiNPs in the pure aqueous solution. This implies that NiNPs independently act as a catalytic additive to enhance CO_2 hydration regardless of the presence of MEA.

3.3. CO_2 absorption by NiNPs and MEA in a long serpentine microchannel

To simulate the higher rate of reactions between CO_2 and the surrounding fluid (i.e., faster mixing than that happened in the microreactor) occurred in the industrial absorbers, we utilized a long serpentine microchannel associated with the visualization of the microbubble flow. It is well known that the flow in most microchannels is in a laminar flow regime characterized as low Reynolds (*Re*) number that induces slow mixing [46,47]. To achieve rapid mixing in a microchannel, a serpentine structure that enhances the mixing of miscible fluid [48] was employed. Fig. 4a shows raw optical images of CO_2 microbubbles generated from the flow-focusing geometry at upstream (far-left) and downstream (far-right) in an aqueous MEA solution. The snapshots of microbubbles at these locations were used to estimate time-dependent changes in bubble diameter. The scattered data points in Fig. 4b is plotted as the changes in non-dimensional microbubble diameter over time. These data points were then curve-fitted to the exponential decay function with an R^2 value of 0.97. To quantify how much the catalytic performance of NiNPs accelerates the CO_2 absorption rate in the aqueous MEA solution, the rate of the change in non-dimensional CO_2 bubble diameter (s^{-1}) was calculated by differentiating the predetermined exponential decay equation with respect to time (Fig. 4c). The average CO_2 absorption rate was determined using values of the rate of the change in non-dimensional CO_2 bubble diameter (s^{-1}) until equilibrium is reached. It should be noted that the catalytic activity of NiNPs enables CO_2 absorption quickly but has no impact on increasing the total amount of CO_2 absorption. The absolute value of the rate of change in non-dimensional CO_2 bubbles diameter was initially determined to be a maximum and its plateau value was observed as time increases.

Fig. 5 shows the results of CO_2 absorption at different MEA concentrations (0, 1.25, 5, 10%) with and without NiNPs at 30 mg/L, respectively. In all experiments, when microbubbles were generated at the junction in the flow-focusing geometry, they were rapidly absorbed into the aqueous phase and have stopped changing their sizes at later times, indicating the reaction reaches equilibrium. In pure water, the CO_2 absorption equilibrium was reached at 2.5 s as shown in Fig. 5a (■). When compared with experiments in the microreactor (Fig. 3a), the time to reach equilibrium is decreased significantly from 200 s to 2.5 s. This implies that the long serpentine microchannel can provide approximately 80-folder higher mixing efficiency than that in the microreactor, which has a great improvement in CO_2 absorption. The final relative change in CO_2 bubble diameter (D/D_0) is decreased from 0.54 to 0.24 at 2.9 s when compared with the control in pure water (■) and 1.25% of aqueous MEA (●) in the high mixing condition.

To better understand the impact of the NiNPs' catalytic activity on

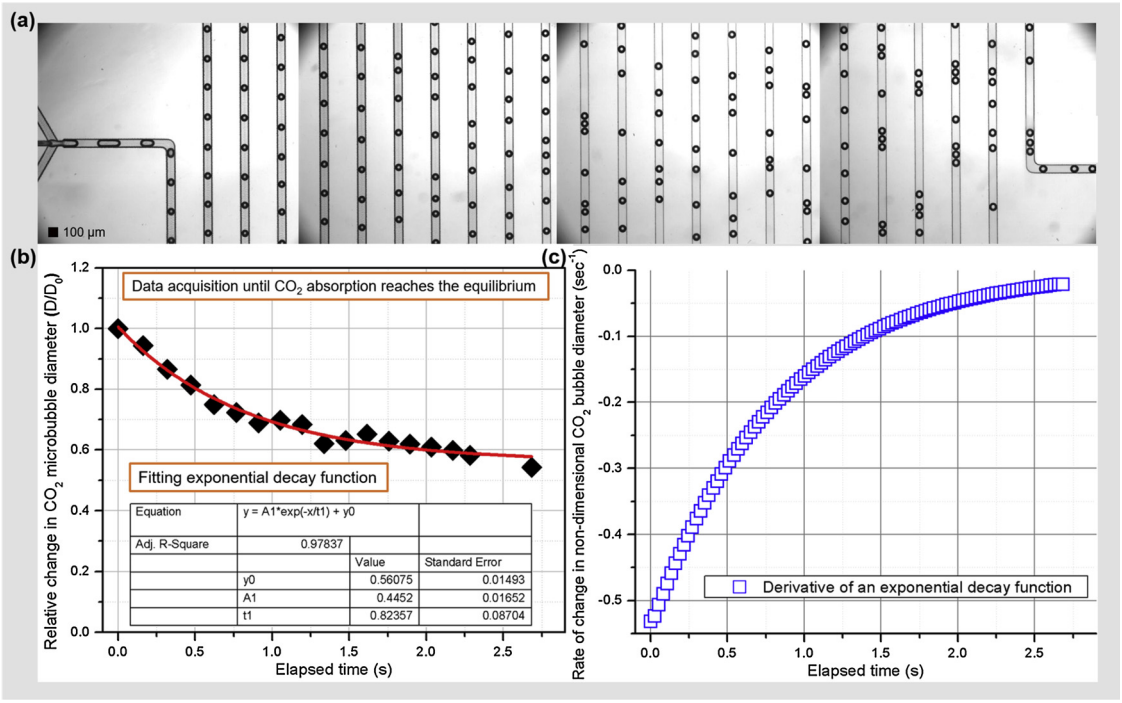

Fig. 4. (**a**) Representative micrographs of CO_2 microbubbles in the long serpentine microchannel in an aqueous-MEA solution: upstream (left) and downstream (right). (**b**) Each black dot represents a relative change in CO_2 microbubble diameter (D/D_0) vs. elapsed time while the red line is a curve-fit of these data to an exponential decay function ($y = 0.56e^{(-x/0.82)} + 0.56$). (**c**) A graph of the rate of change in non-dimensional CO_2 bubble diameter (s^{-1}), determined from the derivative of the exponential decay function (Fig. 4b).

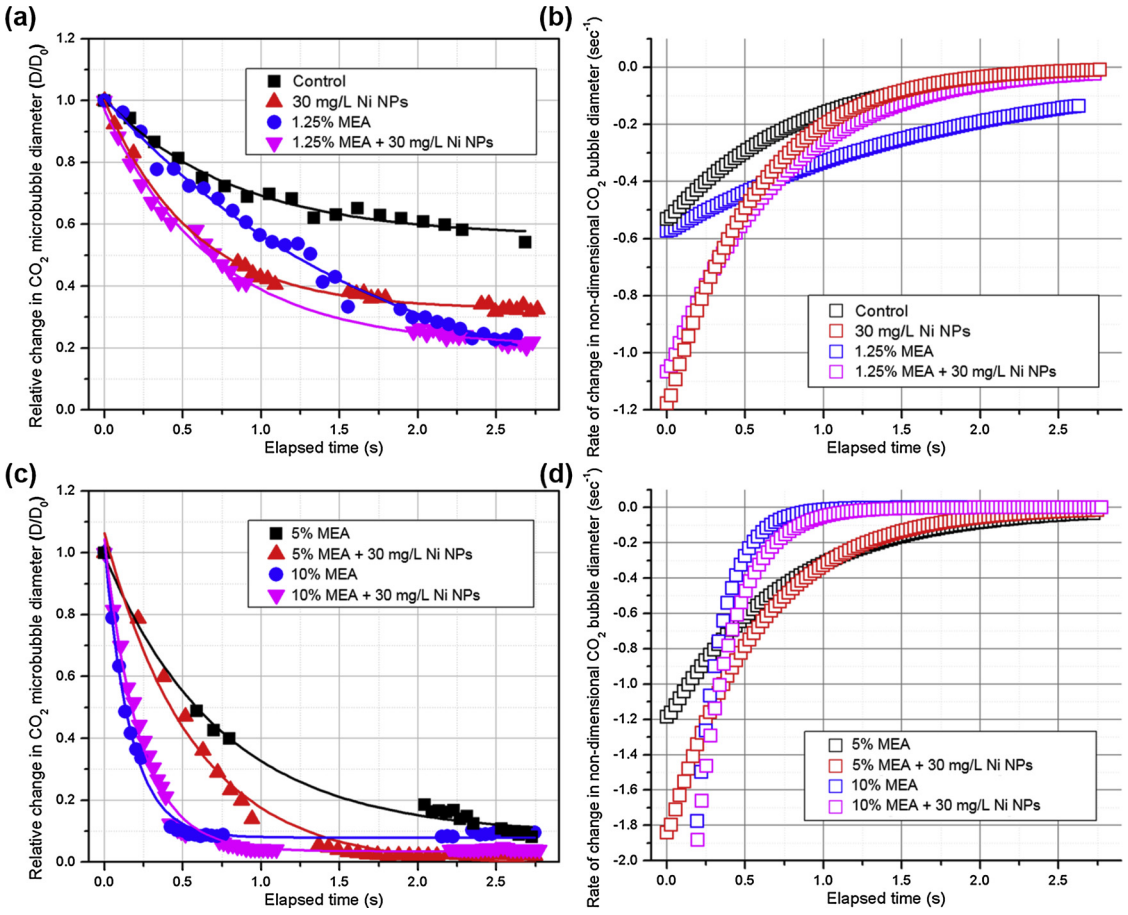

Fig. 5. Graphs of changes in non-dimensional CO_2 bubble diameter (D/D_0) and the corresponding rate of changes in non-dimensional CO_2 bubble diameter (s^{-1}) at different aqueous MEA concentrations at 0% and 1.25% (**a** and **b**) 5% and 10% (**c** and **d**) in the presence and absence of 30 mg L^{-1} NiNPs, respectively.

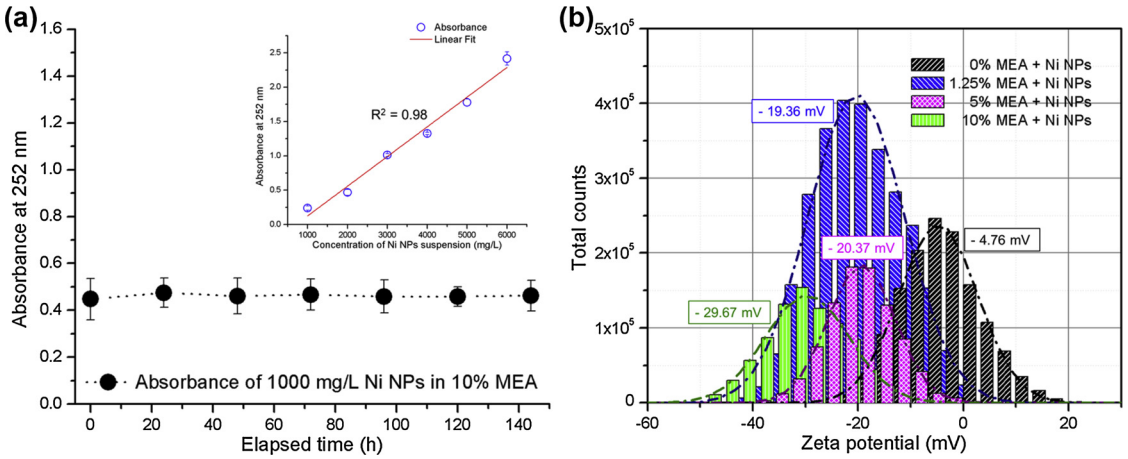

Fig. 6. (**a**) Changes in the concentration of 1000 mg L^{-1} NiNPs in 10% MEA vs. elapsed time over 140 h. The inset figure represents the relationship between absorbance and NiNPs concentration. (**b**) Variations in ζ potential of NiNPs as a function of MEA concentration (0, 1.25, 5, and 10% MEA).

the CO_2 absorption rate, the changes in non-dimensional bubble diameter at different MEA concentrations are plotted in Fig. 5b. The data points in Fig. 5b were determined by differentiating the graphs of relationships between relative change in CO_2 bubble diameter and the elapsed time (Fig. 5a). The initial rates of changes in non-dimensional bubble diameter with NiNPs in the pure water (▲) and 1.25% MEA (▼) are 2-fold higher than those in the absence of NiNPs, respectively. This improvement is presumably because the curved paths in the long serpentine microchannel create a chaotic mixing flow pattern which increases the contact between CO_2 (aq) molecules and NiNPs and leads to an increase in the catalytic activity of NiNPs. As a result, the accelerated rate of the mass transfer of gaseous CO_2 by NiNPs was observed. With a 5% aqueous MEA solution, the relative change in the CO_2 bubble diameter was rapidly decreased over 2.9 s (Fig. 5c, ■). A greater reduction in the size of CO_2 microbubbles at a higher MEA concentration up to 5% was observed, which means the higher MEA concentration allows rapid reaction of CO_2 with the surrounding fluid and therefore increases the degree of bubble shrinkage. At 5% aqueous MEA, NiNPs still perform as catalysts to accelerate the CO_2 absorption rate and thereby lead to a rapidly decreasing rate of non-dimensional bubbles diameter change as shown in Fig. 5d, (■ and ▲). However, at 10% aqueous MEA, the changes in CO_2 bubble diameter and its rates were similar in both the presence and absence of NiNPs (● and ▼). This is because the reaction of MEA with CO_2 is predominant due to the plenty of reactants (MEA) molecules and outweighs the impact of NiNPs. This result suggests that there will be no benefit of using NiNPs for carbon capture in the high mixing condition with high MEA concentrations. The relationship between the change in volume of CO_2 bubbles and the CO_2 absorption rate ($\Delta m/\Delta t$) can be expressed as $\Delta m/\Delta t = \rho_{CO2}\Delta V/\Delta t$, where ρ_{CO2} is the density of CO_2 and ΔV is the change in volume of CO_2 bubbles over time Δt [49]. With a 10% aqueous MEA solution in the presence of NiNPs, the CO_2 absorption rate was determined to be 5×10^{-9} g CO_2/s using 1.77×10^{-9} μm^3 of ΔV, 0.7 s of Δt, and 1.98 kg/m^3 of the density of CO_2. The absorption rate of CO_2 in MDEA-[Bmim][Lys] aqueous solutions is 0.48 g CO_2/100 g aqueous solution/min (8×10^{-5} g CO_2/1 g aqueous solution/s, assuming a linear relationship between the absorption rate and quantity of aqueous solution) [25].

3.4. Compatibility of NiNPs with MEA

The experiment on NiNPs' dissolution in an aqueous MEA solution was conducted to confirm how long NiNPs sustain their catalytic function in the amine-based system. For this purpose, we obtained time-dependent changes in different NiNP concentrations by measuring the absorbance of NiNPs-MEA-aqueous solutions using a spectrophotometer. The absorbance of six different NiNP concentrations were tested in a range from 190 nm to 300 nm. The peak wavelength of NiNPs' absorbance was found to be 252 nm [50]. The NiNPs' absorbance at 252 nm increases linearly with NiNPs concentrations with $R^2 = 0.98$ (Fig. 6a). MEA's absorbance does not interfere with these measurements since the MEA's absorbance peak is at 340 nm [51]. Fig. 6a shows time-dependent changes in absorbance of the aqueous MEA solution containing NiNPs over 140 h. The measurement result shows that any significant dissolution of NiNPs was not observed. Another degradation mechanism of NiNPs' catalytic performance is oxidation. When NiNPs are oxidized, the oxidized Ni metal ion combines with carbonate (CO_3^{2-}) and oxide (O^{2-}) to form Ni(II) carbonate ($NiCO_3$) and Ni(II) oxide (NiO) and their appearance is green crystalline solid. In our tests, oxidation of NiNPs was not observed. Aggregation of NPs could be another source of the degradation of catalytic performance. Fig. 6b shows changes in zeta (ζ) potential at different MEA concentrations. An increase in MEA concentration gradually changes the average ζ potential from -4.76 to -29.67 mV. It is well known when the absolute value of ζ potential is higher than 20 mV, high positive or negative potentials lead to NPs' monodispersity in solution according to DLVO (Derjaguin, Landau, Verwey, and Overbeek) theory [52,53]. Our data show excellent dispersity of NiNPs in the aqueous MEA solution and these dispersed NPs can improve their surface reaction as increasing concentration of aqueous MEA since the efficiency of catalytic activity correlates with the surface-to-volume ratio of NPs [54].

4. Conclusions

This study examined the catalytic performance of NiNPs as a possible additive for improved CO_2 absorption efficiency in the amine-based absorption system. Using two microfluidic platforms that provide efficient controllability of multiphase flows, we were able to evaluate the NiNPs' catalytic CO_2 absorption in an aqueous MEA solution under different mixing conditions, i.e., the limited and high mixing scenarios. We quantified CO_2 absorption through the observation of changes in CO_2 microbubble size. This allowed us to delineate how NiNPs behave under different mixing conditions in terms of CO_2 absorption. In the limited mixing condition, we found that NiNPs maintain notably their catalytic ability because of the NPs' Brownian motion. We found that MEA has no impact on NPs' catalytic performance by measuring NPs' translational diffusion coefficients in pure water and aqueous MEA. We also found that NiNPs accelerate the CO_2-H_2O reaction independently with the reaction of CO_2 with aqueous MEA through a comparative analysis with the absence and presence of NiNPs. On the other hand, the catalytic performance of NiNPs under the high mixing condition was evaluated in the long serpentine microchannel. The catalytic potential of NiNPs accelerates the average CO_2 absorption rate by 34% and 54%

in the limited mixing and the high mixing conditions, respectively. NiNPs can successfully accelerate the required time to reach the CO_2 absorption equilibrium, which means NiNPs can sufficiently reduce the required amount of MEA in the system. The study found that NiNPs can sustain their catalytic function more than 140 h in the amine-based system.

Declaration of competing Interest

The authors declare that they have no known competing financial interests or personal relationships that could have appeared to influence the work reported in this paper.

Acknowledgement

This work was supported by funding from Janke Research Fund at Florida Environmental Studies. We also thank Alexander Shaw, Aubin Joly, Raymond Mathis, Remi Marsac, and Seamus Byrnes for their help with laboratory experiments.

Appendix A. Supplementary data

Supplementary material related to this article can be found, in the online version, at doi:https://doi.org/10.1016/j.jcou.2019.11.011.

References

[1] J.F. Brennecke, B.E. Gurkan, Ionic liquids for CO_2 capture and emission reduction, J. Phys. Che authors declare that they have no known comp m. Lett. 1 (2010) 3459–3464, https://doi.org/10.1021/jz1014828.
[2] F. Su, C. Lu, W. Cnen, H. Bai, J.F. Hwang, Capture of CO_2 from flue gas via multiwalled carbon nanotubes, Sci. Total Environ. 407 (2009) 3017–3023, https://doi.org/10.1016/j.scitotenv.2009.01.007.
[3] M.J. Tuinier, M. van Sint Annaland, G.J. Kramer, J.A.M. Kuipers, Cryogenic CO_2 capture using dynamically operated packed beds, Chem. Eng. Sci. 65 (2010) 114–119, https://doi.org/10.1016/j.ces.2009.01.055.
[4] A. Mansourizadeh, A.F. Ismail, T. Matsuura, Effect of operating conditions on the physical and chemical CO_2 absorption through the PVDF hollow fiber membrane contactor, J. Membr. Sci. 353 (2010) 192–200, https://doi.org/10.1016/j.memsci.2010.02.054.
[5] R.R.P. Noble, L. Stalker, S.A. Wakelin, B. Pejcic, M.I. Leybourne, A.L. Hortle, K. Michael, Biological monitoring for carbon capture and storage – a review and potential future developments, Int. J. Greenh. Gas Control. 10 (2012) 520–535, https://doi.org/10.1016/j.ijggc.2012.07.022.
[6] A.B. Rao, E.S. Rubin, A. Technical, Economic, and Environmental Assessment of Amine-Based CO $_2$Capture Technology for Power Plant Greenhouse Gas Control, Environ. Sci. Technol. 36 (2002) 4467–4475, https://doi.org/10.1021/es0158861.
[7] B. Lv, B. Guo, Z. Zhou, G. Jing, Mechanisms of CO_2 Capture into Monoethanolamine Solution with Different CO_2 Loading during the Absorption/Desorption Processes, Environ. Sci. Technol. 49 (2015) 10728–10735, https://doi.org/10.1021/acs.est.5b02356.
[8] K.-Y.A. Lin, A.-H.A. Park, Effects of bonding types and functional groups on CO_2 capture using novel multiphase systems of liquid-like nanoparticle organic hybrid materials, Environ. Sci. Technol. 45 (2011) 6633–6639, https://doi.org/10.1021/es200146g.
[9] S.B. Hawthorne, A. Kubátová, J.R. Gallagher, J.A. Sorensen, D.J. Miller, Persistence and Biodegradation of Monoethanolamine and 2-Propanolamine at an Abandoned Industrial Site, Environ. Sci. Technol. 39 (2005) 3639–3645, https://doi.org/10.1021/es040556c.
[10] J.-W. Shin, Y.-H. Song, B.-M. An, S.-J. Seo, J.-Y. Park, Energy recovery of ethanolamine in wastewater using an air-cathode microbial fuel cell, Int. Biodeterior. Biodegrad. 95 (2014) 117–121, https://doi.org/10.1016/j.ibiod.2014.05.021.
[11] J.-W. Shin, S.-J. Seo, H.A. Maitlo, J.-Y. Park, The enhancement of ammonium removal from ethanolamine wastewater using air-cathode microbial fuel cells coupled to ferric reduction, Bioresour. Technol. 190 (2015) 466–473, https://doi.org/10.1016/j.biortech.2015.03.048.
[12] S.-J. Seo, J.-W. Shin, H.A. Maitlo, J.-Y. Park, Treatment of ethanolamine using an Fe (III)-based, two-chamber microbial fuel cell with continuous Fe(II) oxidation at the air cathode, J. Chem. Technol. Biotechnol. 91 (2016) 1349–1358, https://doi.org/10.1002/jctb.4731.
[13] Report Buyer, The North America ethanolamine market accounted for a revenue of $794 million in 2017 and is anticipated to generate $1,224 million by 2025, (n.d.). https://www.prnewswire.com/news-releases/the-north-america-ethanolamine-market-accounted-for-a-revenue-of-794-million-in-2017-and-is-anticipated-to-generate-1-224-million-by-2025–300759186.html (accessed February 13, 2019).
[14] Z. Parisheva, A. Demirev, Ozonization of ethanolamine in aqueous medium, Water Res. 34 (2000) 1340–1344, https://doi.org/10.1016/S0043-1354(99)00245-6.
[15] K.-H. Yeon, J.-H. Song, J. Shim, S.-H. Moon, Y.-U. Jeong, H.-Y. Joo, Integrating electrochemical processes with electrodialysis reversal and electro-oxidation to minimize COD and T-N at wastewater treatment facilities of power plants, Desalination. 202 (2007) 400–410, https://doi.org/10.1016/j.desal.2005.12.080.
[16] J.-W. Shin, Y.-H. Song, B.-M. An, S.-J. Seo, J.-Y. Park, Energy recovery of ethanolamine in wastewater using an air-cathode microbial fuel cell, Int. Biodeterior. Biodegrad. 95 (2014) 117–121, https://doi.org/10.1016/j.ibiod.2014.05.021.
[17] J. Anotai, C.-M. Chen, L.M. Bellotindos, M.-C. Lu, Treatment of TFT-LCD wastewater containing ethanolamine by fluidized-bed Fenton technology, Bioresour. Technol. 113 (2012) 272–275, https://doi.org/10.1016/j.biortech.2011.11.100.
[18] S. Horikoshi, N. Watanabe, M. Mukae, H. Hidaka, N. Serpone, Mechanistic examination of the titania photocatalyzed oxidation of ethanolamines, New J. Chem. 25 (2001) 999–1005, https://doi.org/10.1039/b102186i.
[19] A. Filimon, Amino-silicones As Active Compounds In The Detection And Capture Of CO_2 From The Environment Alexandra Bargan And Maria Cazacu, Smart Mater, Integr. Des. Eng. Approaches Potential Appl. (2018), https://doi.org/10.1201/9781351167963-15.
[20] The Dow Chemical Company, Ethanolamines Storage and Handling, (2003) (accessed February 26, 2019), http://msdssearch.dow.com/PublishedLiteratureDOWCOM/dh_0952/0901b803809522f5.pdf?filepath=amines/pdfs/noreg/111-01374.pdf&fromPage=GetDoc.
[21] The Dow Chemical Company, Ethanolamines, (2013) (accessed February 26, 2019), http://msdssearch.dow.com/PublishedLiteratureDOWCOM/dh_0044/0901b8038004475c.pdf?filepath=amines/pdfs/noreg/111-01375.pdf&fromPage=GetDoc.
[22] M.S. Dupart, T.R. Bacon, D.J. Edwards, Understanding corrosion in alkanolamine gas treating plants, Part 1, Hydrocarb. Process. 72 (1993) 75.
[23] M.R.M. Abu-Zahra, L.H.J. Schneiders, J.P.M. Niederer, P.H.M. Feron, G.F. Versteeg, CO_2 capture from power plants, Int. J. Greenh. Gas Control. 1 (2007) 37–46, https://doi.org/10.1016/S1750-5836(06)00007-7.
[24] P. Zhang, X. Tian, D. Fu, CO_2 removal in tray tower by using AAILs activated MDEA aqueous solution, Energy. 161 (2018) 1122–1132, https://doi.org/10.1016/j.energy.2018.07.162.
[25] D. Fu, P. Zhang, L. Wang, Absorption performance of CO_2 in high concentrated [Bmim][Lys]-MDEA aqueous solution, Energy. 113 (2016) 1–8, https://doi.org/10.1016/j.energy.2016.07.049.
[26] D. Fu, P. Zhang, C. Mi, Effects of concentration and viscosity on the absorption of CO_2 in [N1111][Gly] promoted MDEA (methyldiethanolamine) aqueous solution, Energy. 101 (2016) 288–295, https://doi.org/10.1016/j.energy.2016.02.052.
[27] C.A. Lippert, K. Liu, M. Sarma, S.R. Parkin, J.E. Remias, C.M. Brandewie, S.A. Odom, K. Liu, Improving carbon capture from power plant emissions with zinc- and cobalt-based catalysts, Catal. Sci. Technol. 4 (2014) 3620–3625, https://doi.org/10.1039/C4CY00766B.
[28] U.K. Ghosh, S.E. Kentish, G.W. Stevens, Absorption of carbon dioxide into aqueous potassium carbonate promoted by boric acid, Energy Procedia 1 (2009) 1075–1081, https://doi.org/10.1016/j.egypro.2009.01.142.
[29] L.R. Widger, M. Sarma, R.A. Kelsey, C. Risko, C.A. Lippert, S.R. Parkin, K. Liu, Enhancing CO_2 absorption for post-combustion carbon capture via zinc-based biomimetic catalysts in industrially relevant amine solutions, Int. J. Greenh. Gas Control. 85 (2019) 156–165, https://doi.org/10.1016/j.ijggc.2019.04.002.
[30] W. Keim, Nickel: An Element with Wide Application in Industrial Homogeneous Catalysis, Angew. Chem. Int. Ed. Engl. 29 (1990) 235–244, https://doi.org/10.1002/anie.199002351.
[31] B. Dutcher, M. Fan, A.G. Russell, Amine-based CO_2 capture technology development from the beginning of 2013—a review, ACS Appl. Mater. Interfaces 7 (2015) 2137–2148, https://doi.org/10.1021/am507465f.
[32] P. Song, D. Wen, Z.X. Guo, T. Korakianitis, Oxidation investigation of nickel nanoparticles, Phys. Chem. Chem. Phys. 10 (2008) 5057–5065, https://doi.org/10.1039/B800672E.
[33] S. Zhou, S. Wang, C. Chen, Thermal Degradation of Monoethanolamine in CO_2 Capture with Acidic Impurities in Flue Gas, Ind. Eng. Chem. Res. 51 (2012) 2539–2547, https://doi.org/10.1021/ie202214y.
[34] M. Ahmadi, V.G. Gomes, K. Ngian, Advanced modelling in performance optimization for reactive separation in industrial CO_2 removal, Sep. Purif. Technol. 63 (2008) 107–115, https://doi.org/10.1016/j.seppur.2008.04.016.
[35] G.A. Bhaduri, L. Šiller, Nickel nanoparticles catalyse reversible hydration of carbon dioxide for mineralization carbon capture and storage, Catal. Sci. Technol. 3 (2013) 1234, https://doi.org/10.1039/c3cy20791a.
[36] S. Seo, M. Nguyen, M. Mastiani, G. Navarrete, M. Kim, Microbubbles loaded with nickel nanoparticles: a perspective for carbon sequestration, Anal. Chem. 89 (2017) 10827–10833, https://doi.org/10.1021/acs.analchem.7b02205.
[37] S. Seo, G.A. Perez, K. Tewari, X. Comas, M. Kim, Catalytic activity of nickel nanoparticles stabilized by adsorbing polymers for enhanced carbon sequestration, Sci. Rep. 8 (2018), https://doi.org/10.1038/s41598-018-29605-1.
[38] Q. Xu, M. Nakajima, S. Ichikawa, N. Nakamura, P. Roy, H. Okadome, T. Shiina, Effects of surfactant and electrolyte concentrations on bubble formation and stabilization, J. Colloid Interface Sci. 332 (2009) 208–214, https://doi.org/10.1016/j.jcis.2008.12.044.
[39] R.M. Noyes, M.B. Rubin, P.G. Bowers, Transport of carbon dioxide between the Gas Phase and water under well-stirred conditions: rate constants and mass accommodation coefficients, J. Phys. Chem. 100 (1996) 4167–4172, https://doi.org/10.1021/jp952382e.
[40] J.R. Howse, R.A.L. Jones, A.J. Ryan, T. Gough, R. Vafabakhsh, R. Golestanian, Self-motile colloidal particles: from directed propulsion to random walk, Phys. Rev. Lett. 99 (2007) 048102, , https://doi.org/10.1103/PhysRevLett.99.048102.
[41] D. Du, E. Hilou, S. Lisa Biswal, Reconfigurable paramagnetic microswimmers:

Brownian motion affects non-reciprocal actuation, Soft Matter 14 (2018) 3463–3470, https://doi.org/10.1039/C8SM00069G.
[42] P.V. Danckwerts, The reaction of CO_2 with ethanolamines, Chem. Eng. Sci. 34 (1979) 443–446, https://doi.org/10.1016/0009-2509(79)85087-3.
[43] Caplow Michael, Kinetics of carbamate formation and breakdown, J. Am. Chem. Soc. 90 (1968) 6795–6803, https://doi.org/10.1021/ja01026a041.
[44] P.V. Danckwerts, The reaction of CO_2 with ethanolamines, Chem. Eng. Sci. 34 (1979) 443–446, https://doi.org/10.1016/0009-2509(79)85087-3.
[45] Michael. Caplow, Kinetics of carbamate formation and breakdown, J. Am. Chem. Soc. 90 (1968) 6795–6803, https://doi.org/10.1021/ja01026a041.
[46] X. Mao, B.K. Juluri, M.I. Lapsley, Z.S. Stratton, T.J. Huang, Milliseconds microfluidic chaotic bubble mixer, Microfluid. Nanofluidics 8 (2010) 139–144, https://doi.org/10.1007/s10404-009-0496-4.
[47] G.R. Wang, F. Yang, W. Zhao, There can be turbulence in microfluidics at low Reynolds number, Lab Chip 14 (2014) 1452–1458, https://doi.org/10.1039/C3LC51403J.
[48] L. Zheng, G. Cai, S. Wang, M. Liao, Y. Li, J. Lin, A microfluidic colorimetric biosensor for rapid detection of Escherichia coli O157:H7 using gold nanoparticle aggregation and smart phone imaging, Biosens. Bioelectron. 124–125 (2019) 143–149, https://doi.org/10.1016/j.bios.2018.10.006.
[49] M. Sauzade, T. Cubaud, Initial microfluidic dissolution regime of CO_2 bubbles in viscous oils, Phys. Rev. E 88 (2013) 051001, , https://doi.org/10.1103/PhysRevE.88.051001.
[50] S. Schuermans, T. Maurer, J. Martin, J.-B. Moussy, J. Plain, Plasmon / interband transitions coupling in the UV from large scale nanostructured Ni films, Opt. Mater. Express 7 (2017) 1787–1793, https://doi.org/10.1364/OME.7.001787.
[51] K.K. Ngim, J. Zynger, B. Downey, Analysis of Monoethanolamine by Derivatization with Marfey's Reagent and HPLC, J. Chromatogr. Sci. 45 (2007) 126–130, https://doi.org/10.1093/chromsci/45.3.126.
[52] B. Derjaguin, L. Landau, Theory of the stability of strongly charged lyophobic sols and of the adhesion of strongly charged particles in solutions of electrolytes, Prog. Surf. Sci. 43 (1993) 30–59, https://doi.org/10.1016/0079-6816(93)90013-L.
[53] E.J.W. Verwey, Theory of the Stability of Lyophobic Colloids, J. Phys. Colloid Chem. 51 (1947) 631–636, https://doi.org/10.1021/j150453a001.
[54] C. Burda, X. Chen, R. Narayanan, M.A. El-Sayed, Chemistry and properties of nanocrystals of different shapes, Chem. Rev. 105 (2005) 1025–1102, https://doi.org/10.1021/cr030063a.